

## Single-objective selective-volume illumination microscopy enables high-contrast light-field imaging: supplement

SARA MADAAN,<sup>1,2,†</sup> KEVIN KEOMANEE-DIZON,<sup>1,†</sup> MATT JONES,<sup>1</sup>  
CHENYANG ZHONG,<sup>1</sup> ANNA NADTOCHIY,<sup>1</sup> PETER LUU,<sup>1</sup> SCOTT E.  
FRASER,<sup>1</sup> AND THAI V. TRUONG<sup>1,\*</sup> 

<sup>1</sup>*Translational Imaging Center, University of Southern California, Los Angeles, California 90089, USA*

<sup>2</sup>*Current address: Google Inc., Mountain View, California 94043, USA*

\*Corresponding author: [tvtruong@usc.edu](mailto:tvtruong@usc.edu)

†These authors contributed equally to this Letter.

---

This supplement published with The Optical Society on 9 June 2021 by The Authors under the terms of the [Creative Commons Attribution 4.0 License](https://creativecommons.org/licenses/by/4.0/) in the format provided by the authors and unedited. Further distribution of this work must maintain attribution to the author(s) and the published article's title, journal citation, and DOI.

Supplement DOI: <https://doi.org/10.6084/m9.figshare.14604657>

Parent Article DOI: <https://doi.org/10.1364/OL.413849>

# Single-objective selective-volume illumination microscopy enables high-contrast light-field imaging: supplementary material

## 1. Microscope optics

### 1.1 ASO-SVIM: oblique-angled one-photon excitation and wide-field illumination modes

Fig. S1. Simplified schematic diagram of ASO-SVIM

### 1.2 2P-ASO-SVIM: two-photon excitation mode

### 1.3 Improving the signal rate and volumetric imaging speed of 2P-ASO-SVIM

### 1.4 Light-field detection and reconstruction

Fig. S2. 3D opto-mechanical model of the ASO-SVIM light-field detection path

### 1.5 Tradeoffs associated with light-field detection in ASO-SVIM

### 1.6 SPIM: one-photon and two-photon light-sheet imaging modes

### 1.7 Instrument control

### 1.8 Characterizing system resolution

Fig. S3. System resolution

## 2. $k$ -space filtering

Fig. S4.  $k$ -space filtering algorithm

Fig. S5.  $k$ -space filtering reduces artifacts and improves volume reconstruction with uncompromised resolution

Fig. S6.  $k$ -space filtering improves volume reconstruction quality *in vivo*

Fig. S7. ASO-SVIM enhances effective resolution across large tissue volumes

Fig. S8. Comparison of line cuts through vessel structures *in vivo*

Fig. S9. ASO-SVIM enables high-throughput imaging of whole-brain blood flow in zebrafish larvae

Captions for Visualizations 1 to 4

References

## 1. Microscope optics

We describe here the light-field-based selective-volume illumination microscope used in our work. Refer to Fig. S1 for the beam paths and key components.

### 1.1 ASO-SVIM: oblique-angled one-photon excitation and wide-field illumination modes

The illumination path for one-photon (1P) excitation, represented by the blue line, is provided by a bank of continuous-wave (CW) fiber lasers (Coherent OBIS LX, UFC Galaxy: 488 nm, 30 mW; 514 nm, 50 mW; 640 nm, 75 mW) and high-power CW lasers (488 nm, 300 mW, Coherent Sapphire LP; and 532 nm, 5 W, Coherent Verdi). Light from the CW laser bank is collimated and expanded by an objective (BE; Nikon, Plan Fluorite 10 $\times$ , 0.3 NA, 16 mm WD), directed by a dichroic mirror (DC1; FF750-SDi02-25x36, Semrock), and passed through a remote refocus module, which is composed of lens pair T<sub>1</sub> and T<sub>2</sub> (both 75-mm focal length, Thorlabs AC254-075-A-ML). Adjusting the position of T<sub>2</sub> refocuses the beam waist so that it is coincident to the nominal detection focal plane at the sample. The illumination beam is then sent to a 2D ( $x$ - $y$ ) scanning galvo system (G; 6-mm aperture silver mirrors, Cambridge Technology H8363) before being passed through a scan lens (SL; 110-mm focal length, Thorlabs LSM05-BB), a tube lens (TL; 150-mm focal length, Thorlabs AC508-150-B), and a water-dipping objective (ASO; Nikon, CFI LWD Plan Fluorite 16 $\times$ , 0.8 NA, 3 mm WD); G, SL, and TL are mounted on a computer-controlled motorized translational stage (Newport 436 and Newport LTA-HS) to control the inclination angle in ASO-SVIM mode (tilted 26.5° relative to the optical axis of ASO; purple dashed line), and easily port the beam back to the wide-field illumination mode. The illumination NA is adjusted to be  $\sim 0.04$  to 0.06, depending on the selective illumination extent, yielding a fluorescence Gaussian-beam waist of  $\sim 4$  to 6  $\mu\text{m}$  with an axial ( $z$ ) extent ranging from  $\sim 150$  to 230  $\mu\text{m}$  (measured as the confocal parameter of the focal volume). As G is conjugate to the back pupil of ASO, scanning along the  $x$ - and  $y$ -axes with the appropriate voltages selectively paints out the desired sample volume.

For fast volumetric 1P imaging, the high-power CW laser was used to provide the high laser intensity needed beyond what the CW laser bank could provide. Light from the high-power CW lasers are collimated and expanded by BE (Thorlabs BE052-A) and directed by mirrors to a cylindrical beam-shaping module, composed of a pair of cylindrical lenses C<sub>1</sub> and C<sub>2</sub> (-50-mm focal length, Thorlabs LK1662L1 or -30-mm focal length, Thorlabs LK1982L1; and 150-mm focal length, Thorlabs LJ1629L1) which expand the beam elliptically in the  $y$ -direction. This expanded beam is reflected by a mirror mounted on a motorized motion-control stage (MM1; Newport 436 and Newport LTA-HS), where it is directed through T<sub>1</sub> and T<sub>2</sub> and then focused into a 2D ( $y$ - $z$ ) sheet by C<sub>3</sub> (75-mm focal length, Thorlabs LJ703RM-A) onto G. Thus, G only needs to provide scanning along the  $x$ -axis to selectively paint out the desired volume at the sample. Note that C<sub>3</sub> is used only for 1D scanning, and omitted in the other imaging modes. All 1P imaging data were acquired with 1D scanning except for Fig. 3, where 2D scanning was employed to provide a more precise selectively-illuminated volume, in order to avoid direct illumination of the animal's eyes. An inspection camera (not shown; PCO pco.edge 5.5) conjugate to the sample volume and coincident to the  $x$ - $z$  plane aided in alignment and calibration of the illumination tilt angle and G scanning parameters. Tradeoffs associated with volume-scanning as well as alternative implementations of selective-volume illumination are discussed in [1].

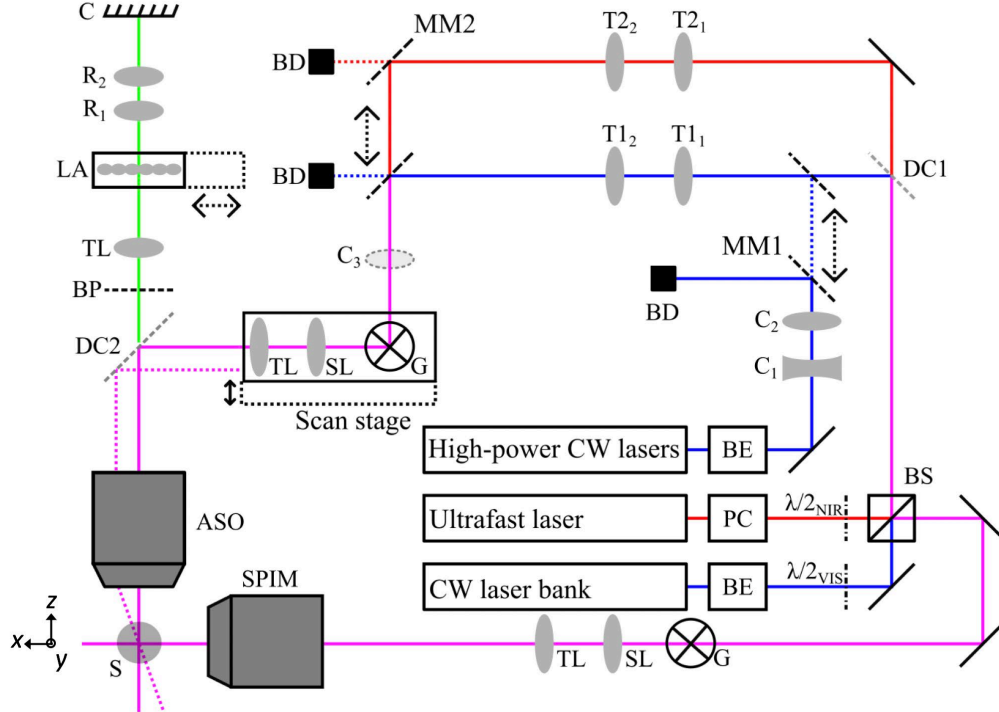


Fig. S1. Simplified schematic diagram of ASO-SVIM. CW: continuous-wave; BE: beam expander; PC: Pockels cell;  $\lambda/2$ : half-wave plate, where the subscripts VIS and NIR refer to the visible and near-infrared wavelengths, respectively; BS: polarizing beamsplitter; DC: dichroic mirror; T1: VIS relay lens, T2: NIR relay lens, C: VIS cylindrical lens, MM: movable mirror, where the subscripts refer to the sequence of elements; BD: beam dump; G: 2D scanning galvo mirrors; SL: scan lens; TL: tube lens; ASO: ASO-SVIM objective; SPIM: light-sheet excitation objective; S: sample; BP: band-pass filter; LA: lenslet array; R: detection relay lens, where the subscripts refer to the sequence of lenses; C: camera sensor.

### 1.2 2P-ASO-SVIM: two-photon excitation mode

The illumination path for two-photon (2P) excitation begins in red. Near-infrared (NIR) pulsed illumination is provided by a Ti:Sapphire ultrafast laser (Coherent Chameleon Ultra II) and the illumination power is controlled by a Pockels cell (PC; Conoptics 350-80). A polarizing beamsplitter (PBS; Thorlabs PBS102) is used to combine the visible and NIR beams into a co-linear beam and to split the combined beam into two integrated excitation paths (towards ASO and SPIM objectives). Visible and NIR half-wave plates ( $\lambda/2_{\text{VIS}}$  and  $\lambda/2_{\text{NIR}}$ ; Thorlabs AHWP05M-600 and AHWP05M-980), each mounted in manual rotation mounts, are used to adjust the laser power delivered to ASO and SPIM as appropriate. In the ASO path, the NIR illumination beam is transmitted through DC1 and then through lens pair T<sub>1</sub> and T<sub>2</sub> (75-mm focal length, Thorlabs AC254-75-B-ML and 100-mm focal length, Thorlabs AC254-100-B), used to expand and refocus the beam waist before being sent to the same illumination-scanning optics in the aforementioned 1P mode (G, SL, TL, and ASO). A mirror mounted on a motion-control stage (MM2) allows automated switching between 2P- and 1P-ASO excitation. The illumination NA is adjusted to be  $\sim 0.055$  to  $0.08$ , yielding similar fluorescence Gaussian-beam characteristics as the 1P mode:  $\sim 4$  to  $5 \mu\text{m}$  waist and  $\sim 150$  to  $230 \mu\text{m}$  axial extent. For all 2P imaging experiments presented (Figs. 2-3),  $\sim 525 \text{ mW}$  of average laser power was delivered to the specimen. Although we did not observe any photodamage in live imaging of zebrafish larvae, a quantitative assessment of the excitation laser power on photobleaching and sample health is needed for prolonged biological experiments.

### *1.3 Improving the signal rate and volumetric imaging speed of 2P-ASO-SVIM*

In our work, we did not try to maximize the volumetric imaging rate of 2P-ASO-SVIM (or any of the other compared modalities), including for the neuro imaging demonstration, as shown in Fig. 3. The main reason was that we would like to focus on comparing how the different background levels affect the image quality of the various modalities. Thus we have used exposure times generally longer than needed to ensure that the overall brightness of the images was not a limiting factor in the comparison. The second reason, specific to the neuro imaging, was that given the relatively slow dynamics of the nuclear-localized GCaMP6s calcium indicators ( $\approx 1$  s), the 1 vol/s imaging rate was adequate in capturing the relevant neuronal firings in the zebrafish brain, as demonstrated in Fig. 3c. Judging from the signal-to-noise ratio obtained in the 2P-ASO-SVIM data, we deem that the exposure could have been reduced by a factor of 2 or more, thus yielding a volumetric rate of 2 vol/s or more, and the resulting signal-to-noise would still have been sufficient. Despite the fact that our work is not aimed at maximizing the volumetric imaging rate of 2P-ASO-SVIM, it is useful to consider potential measures that could bring improvements toward that direction. We describe these measures below.

The optical train of our current 2P-ASO-SVIM setup leaves room for improvement, as there are a number of potentially dispersive optical elements, including the high-NA primary objective used for excitation/detection (Fig. S1). The resulting dispersion could broaden the ultrafast pulse width, reducing the signal for a given laser power (since the signal scales inversely with pulse width), thereby reducing the volumetric imaging rate. Thus, one future improvement would be to implement dispersion compensation to restore the ultrafast pulse back to its bandwidth-limited duration [2].

In 2P point-scanning microscopy, fast resonant scanners have been found to reduce photodamage when used in “time-averaged” mode, where the recorded image comes from the average signal of the sample being scanned multiple times, as compared to when the sample is scanned only once with a  $\sim 10$ -fold slower galvanometer scanner, both under identical average excitation power. This comes from the fact that the faster scanning allows the laser beam to illuminate a given voxel within the sample multiple times in accumulating the signal, increasing the illumination duty cycle, spreading the laser excitation out over time, and thus reducing photodamage. Since 2P-ASO-SVIM also employs beam scanning to illuminate the selective volume of interest, we expect that by using a resonant scanner, instead of the current galvanometer scanner currently used in our setup, we could reduce the photodamage, which in turn would allow us to increase the laser power to increase the signal rate and thus the volumetric imaging rate.

Finally, it has recently been shown that the signal rate of two-photon light sheet microscopy (2P-SPIM), a modality that 2P-ASO-SVIM shares the beam-scanning illumination strategy with, can be increased by an order of magnitude by lowering the ultrafast laser pulse repetition rate to 1-40 MHz, in contrast to the standard 80 MHz of lasers typically used in multiphoton microscopy [3]. The low repetition rate permits higher peak intensity at a constant average power, leading to a higher signal rate due to the squared-dependence of the signal on the peak intensity, while limiting thermal toxicity from linear absorption. Note that since both 2P-SPIM and 2P-ASO-SVIM use a low-numerical-aperture focused beam for illumination, the peak intensity is typically  $\sim 100$  times lower than conventional 2P point-scanning microscopy, and therefore there is significant overhead room for the peak intensity to be increased, with the lower repetition rate, before nonlinear photodamage starts to become a problem. Thus, we envision that similar to the results shown for 2P-SPIM in [3], a lower ultrafast laser repetition rate would enhance the signal rate and volumetric imaging speed of 2P-ASO-SVIM.

### *1.4 Light-field detection and reconstruction*

Excited fluorescence at the sample is collected by the ASO objective. A dichroic mirror (DC2; Di01-R488/561 or di01-R405/488/543/635-25x36) and a filter wheel (Sutter Instrument

Lambda 10-3, 32 mm diameter) equipped with emission filters (FF01-470/28-32, FF03-525/50-32, FF01-609/54-32, and FF01-680/42-32) together block the excitation light and transmit the fluorescence signal emitted from the sample (green). An intermediate image at an overall magnification of  $24\times$  is projected onto a lenslet array (LA; 2.06-mm focal length,  $18\times 18$  mm,  $136\ \mu\text{m}$  pitch, AR coated, OKO Technologies APO-Q-P192-F3.17; f-number matched to the NA of ASO) by a tube lens (TL; 300-mm focal length, Edmund Optics 88-597). With LA placed at the native image plane, an array of fluorescence focal spots is created, which encode 4D spatio-angular information for each position in the 3D volume—referred to as the light-field [4,5]. The generated light-field is imaged onto an sCMOS camera (C; Andor Zyla 5.5) by a pair of photographic lenses  $R_1$  and  $R_2$  (both 50-mm focal length, Nikon NIKKOR f/1.4). These raw light-fields are reconstructed into full volumes as described in refs. [1,6]. Unless otherwise noted, all image stacks are further processed using a filtering algorithm described in Section 2.

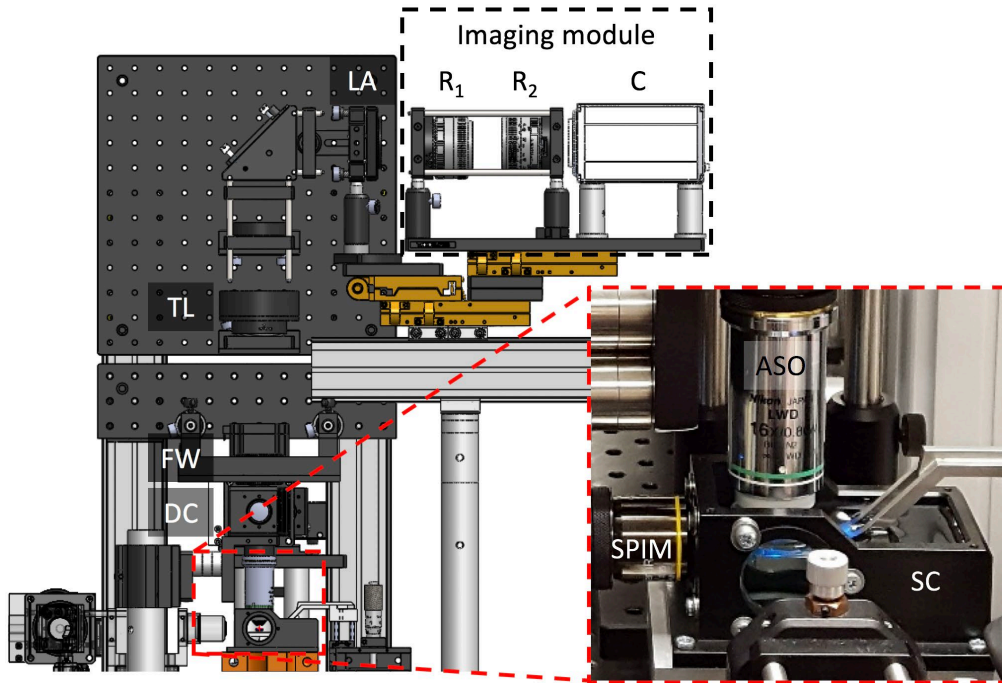


Fig. S2. 3D opto-mechanical model of the ASO-SVIM light-field detection path. Inset shows a photograph of the sample chamber, the axial-single-objective (ASO) used to both deliver selective-volume illumination at the sample and collect the excited fluorescence, as well as the light-sheet excitation objective (SPIM). Owing to the ASO design, samples can be mounted using a caddy and dive bar system as described in ref. [7] and are entirely compatible with standard sample preparation protocols (e.g., Fig. S9). Fluorescence collected from ASO passes through a dichroic mirror (DC), a filter wheel (FW), a tube lens (TL), a lenslet array (LA), and onto an imaging module. R: detection relay lens, where the subscripts refer to the sequence of lenses; C: camera.

### 1.5 Tradeoffs associated with light-field detection in ASO-SVIM

For opto-mechanical convenience and simplicity, we designed our light-field detection arm in an upright epi-configuration [Fig. 1(A) and Fig. S2]. In 2P-ASO-SVIM, we illuminate the sample volume axially with a low NA Gaussian beam [Fig. 1(E)], capturing the full cone of light from the ASO objective: maximizing spatio-angular information, sensitivity, and the usable volume. Axial 2P illumination has the additional benefit of defining the volume of interest axially, owing to the quadratic dependence of the signal on the laser intensity, greatly suppressing extraneous background and providing exceptional contrast. In 1P-ASO-SVIM, we obliquely illuminate the sample volume at a tilt angle of  $26.5^\circ$  to the optical axis [Fig. 1(D)].

This similarly captures the full cone of light admitted by the ASO objective as 2P-ASO-SVIM, but does not fully eliminate out-of-volume background because the illuminated volume is larger than the desired detection volume, resulting in residual background above and below the volume of interest, thus leading to 1P-ASO-SVIM performing less well in enhancing the contrast than the ideal performance of the previously reported orthogonal SVIM [1], which of course requires two orthogonal microscope objectives.

In future work, to enhance the background-elimination of 1P-ASO-SVIM, we generally want to increase the inclination angle between the illumination and detection axes, toward the orthogonal condition of being equal to  $90^\circ$ , to more fully leverage the geometry for selective illumination. A simple way to achieve this would be to use an ASO objective with higher NA to enable a larger inclination angle between the illumination and detection axes, which then would reduce the illuminated  $z$ -extent above and below the desired detection volume, and thus lead to lower extraneous out-of-volume background. Another way to increase the angle between the illumination and detection axes is by borrowing a strategy from single-objective implementations of light-sheet microscopy, where a tertiary imaging module is employed to tilt the detection axis so that it is  $\sim 90^\circ$  to the illumination beam [8-10]. Nonetheless, while the tilted detection path would indeed produce less background, the usable field of view and light collection efficiency of the primary objective would be compromised, limiting resolution and sensitivity. Recent developments in single-objective light-sheet microscopy have shown promise in preserving much of the full NA of the primary objective by compressing the light cone angle between an index-mismatched pair of objectives in a tilted tertiary imaging module [11-13]. This concept could certainly be combined with ASO-SVIM to circumvent the reduced NA in a tilted light-field detection configuration and extend the improvements in contrast.

### *1.6 SPIM: one-photon and two-photon light-sheet imaging modes*

In order to operate in SPIM mode, either  $\lambda/2_{\text{VIS}}$  or  $\lambda/2_{\text{NIR}}$  is rotated so that enough excitation energy is transmitted through PBS and delivered at the sample. After PBS, the illumination beam is routed to a 2D ( $x$ - $z$ ) scanning galvo system (G; 5-mm aperture silver mirrors, Thorlabs GVSM002), and then passed through SL, TL, and an objective (SPIM; Olympus, LMPLN-IR 10 $\times$ , 0.3 NA, 18 mm WD) to excite the sample with a scanned Gaussian-beam light-sheet. The SPIM objective is mounted on a manual translational stage to create more sample space for ASO-SVIM mode if needed.

In order to collect images in SPIM mode, LA is moved entirely out of the detection path, and the entire imaging module (R1, R2, and C) is moved in  $-z$  by the focal length of LA. As shown in Fig. S2, LA and the imaging module are each mounted on motorized linear translational stages (Newport 436 and Newport LTA-HS), enabling high-precision positioning and seamless switching between light-field and conventional wide-field/SPIM detection via computer command. The stages also serve to aid in fine alignment. To assemble a 3D volume, 2D images are recorded in series by scanning the sample in  $z$  through the stationary light-sheet with a motorized stage (Newport 436 and Newport LTA-HS).

In the comparison of the imaging modalities presented in Fig. 2, where SPIM was used to provide the ground-truth images, the 3D volume was recorded with 67  $z$ -slices, spaced 1.5 microns apart, with an exposure time of 0.355 s for each slice, yielding a total acquisition time of 44 s. Note that this final total time included the overhead time associated with the  $z$ -stack acquisition (such as stage moving and settling time, and communication overhead). For the corresponding 1P- and 2P-ASO-SVIM recordings, we used an exposure time of 0.355 s for the single snapshot required to capture the 3D volume. This single snapshot was then reconstructed to achieve the final 3D volume, where the  $z$ -step size was set to be 2 microns during the reconstruction process. The total time needed to record the 3D volume, 44 s and 0.355 s, for SPIM and ASO-SPIM, respectively, demonstrate that ASO-SVIM is  $\sim 100$  times faster than SPIM in volumetric imaging.

A comprehensive comparison of the volumetric imaging speed between ASO-SVIM and SPIM would require additional details, such as adjusting the respective exposure times to equalize the signal-to-noise ratios, and considerations for the different resolutions between the two modalities. Such an in-depth comparison has been carried out in our previous report on SVIM [1, Supplementary Note 2]. Importantly, ASO-SVIM is expected to perform similarly to SVIM in terms of the volumetric imaging rate, as the main difference between them is in the illumination direction, which should not affect the imaging speed.

### ***1.7 Instrument control***

Instrument control is similar to our previous implementation [1], with the primary changes concerning the coordination between the scanning system and camera triggering. In our new single-objective configuration, a combination of custom software developed in LabView (National Instruments), ScanImage [14], and Micro-Manager [15] synchronize the scanning system, laser intensity, and camera triggering so that the volume of interest is illuminated an integer number of times within one camera exposure and the excitation intensity is near-uniform frame-to-frame during acquisition. All the motorized linear translational stages used to switch between modes are controlled by an XPS Universal Motion Controller (Newport XPS-Q8). The 3D stage stack-up (Sutter MP-285) used for sample positioning is controlled with its corresponding controller; the sample-scanning  $z$ -stage (noted in Section 1.4) is controlled via Micro-Manager.

### ***1.8 Characterizing system resolution***

To quantify resolution in volumetric reconstructions of light-fields, we measured the point-spread function (PSF) with 175-nm fluorescent beads sparsely suspended in agarose (Fig. S3). We stepped the sparse bead sample in  $z$  by 2  $\mu\text{m}$  over a 200- $\mu\text{m}$  volume, imaging the same field of beads at different axial depths, and thereby facilitating multiple measurements of isolated beads throughout the light-field volume. The  $z$ -series of light-field images were then reconstructed to yield a series of 3D-stacks with overlapping  $z$ -extents, from which we calculated the resolution as a function of relative  $z$ -depth (Fig. S3B). The observed relation between relative  $z$ -depth and the PSF are consistent with results derived from wave optics theory [5]: at different axial depths, the PSF size is different, generally broadening away from the native focus symmetrically; on the other hand, bead-measured PSFs across reconstructed 2D ( $x$ - $y$ ) slices at each corresponding  $z$ -depth are nearly identical.

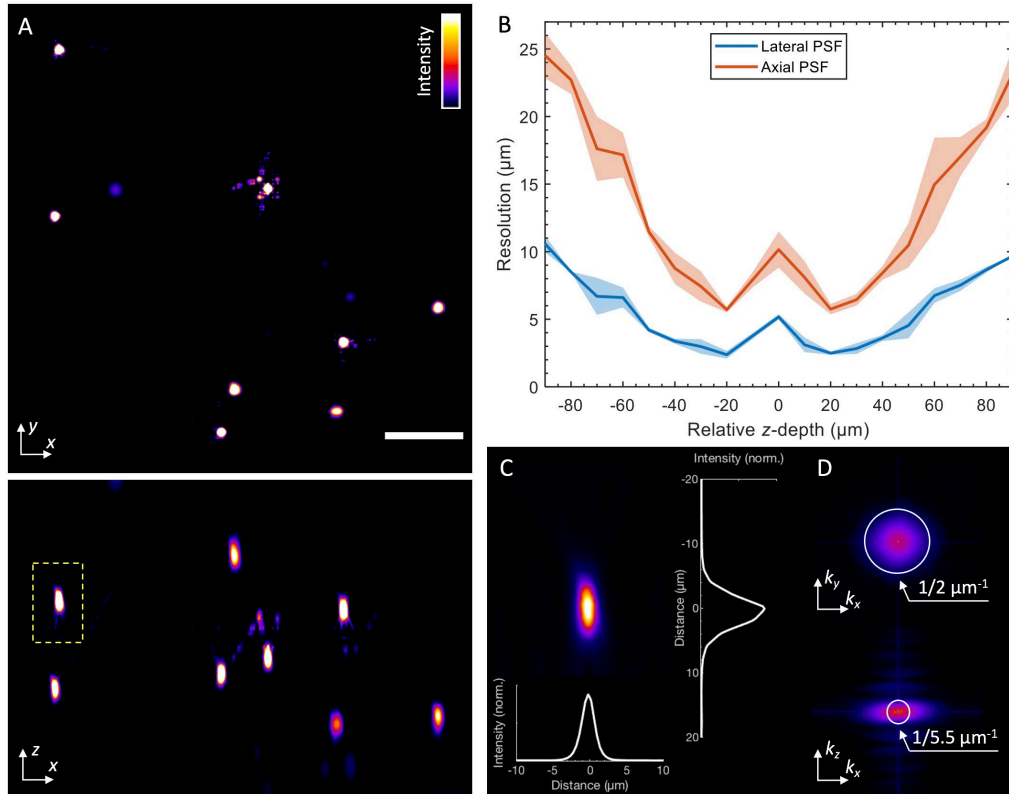


Fig. S3. System resolution. (A)  $x$ - $y$  (top) and  $x$ - $z$  (bottom) maximum-intensity projections (MIPs) of a 300- by 300- by 200- $\mu\text{m}$  field of beads in agarose. Scale bar, 50  $\mu\text{m}$ . (B) Lateral ( $x$ - $y$ ) and axial ( $x$ - $z$ ) PSF measurements across the imaging volume, where  $z = 0$  is the native focus ( $N = 53$  FWHM bead images at different depths). Means (center lines) and standard deviations (shadings) are shown. (C) Enlarged view of the  $x$ - $z$  MIP of an exemplary bead from the image volume, denoted by dashed yellow rectangle (in A, bottom). Line profiles of the lateral (bottom) and axial (right) intensities through the center of the bead. Note that MIPs are contrast adjusted (0.4% of the pixels are saturated), separately for (C) and (A), so the image of the selected (dashed rectangle) bead may appear different. (D) Same bead presented as lateral (top) and axial (bottom) views of the optical transfer functions with resolution bands (white circles).

## 2. *k*-space filtering

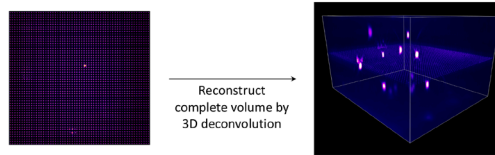
We describe here our *k*-space filtering process to alleviate light-field microscopy (LFM) reconstruction artifacts. These grid-like artifacts are due to the degeneracy in spatio-angular sampling at the native focal plane, and have been described theoretically and experimentally [5]. Our method is motivated by two empirical observations. First, the grid-like artifacts are mainly composed of spatial frequencies beyond the theoretical resolution limit of the detection optics (Fig. S5A, left column). Second, the artifacts are most prominent at the native focal plane and the immediate axial range around it (Fig. S5B, left column and Fig. S6C). With these observations in mind, we devised the following filtering procedure that selectively removes the bulk of reconstruction artifacts without compromising the resolution of the 3D volume.

At the native focal plane, the theoretical maximum lateral resolution is determined by the diffraction-limited sampling rate of LA: the lenslet pitch divided by the effective magnification [5], which we experimentally confirmed (theory: 5.7  $\mu\text{m}$ ; experiment:  $5.2 \pm 0.2 \mu\text{m}$ ). This resolution limit sets a cutoff frequency in Fourier space (*k*-space) where we can impose a low-pass filter to remove high-frequency noise, the main source of the image artifacts (Fig. S5A, left column). We apply this low-pass filter to the native focal plane and adjacent planes extending across a 10- $\mu\text{m}$  depth, a small subvolume defined by the experimental axial PSF (see dashed yellow rectangles in Fig. S5B). Image planes outside of this subvolume are not low-pass filtered. Note that in LFM the resolution changes as a function of depth, and maximum resolution is achieved at *z* positions away from the native focal plane [5], as experimentally shown in Fig. S3B. Because only the subvolume that extends across the focal plane (where artifacts are most prominent) is *k*-space filtered, higher resolution present elsewhere in the volume is unscathed. Experimental aberrations, background, scattering, and other sources of noise break the underlying assumptions in the reconstruction [1,5], generally decreasing the highest non-zero spatial frequency achievable (i.e., the *effective* resolution limit)—or artificially increasing it—making our *k*-space filter a conservative approach. Our filtering process is outlined in Fig. S4 and can be combined with any LFM reconstruction algorithm.

To quantitatively assess how well *k*-space filtering mitigates reconstruction artifacts, we compared standard LFM and *k*-space filtered reconstructions of a 300- by 200- by 200- $\mu\text{m}$  field of beads in agarose (Fig. S5). In large part the field of beads are similar, but it's clear that artifacts are visible both in lateral and axial maximum-intensity projection (MIP) views of the conventional reconstruction that are not apparent with *k*-space filtering (Fig. S5A). Even though the periodic artifacts are only concentrated at the native focus (Fig. S5B, left column), they persist and lift the noise floor throughout the lateral MIP view (Fig. S5A, left column). High-frequency artifacts can swamp the signal intensity of weak point sources, making it difficult to differentiate artifacts from real signal; in contrast, the *k*-space filtered signal intensities are weighted as expected—where real point sources are located (Fig. S5D, line 2). In addition, filtering significantly decreases reconstruction artifacts without any loss of spatial resolution throughout the 3D volume, as measured by line cuts through several PSFs (Fig. S5D, line 1).

We further tested *k*-space filtering *in vivo*, where background and noise can critically affect the reconstruction quality [1]. We acquired volumetric data of transgenic zebrafish embryos expressing green fluorescent protein in the cranial vasculature by means of LFM and light-sheet microscopy (also known as selective-plane illumination microscopy; SPIM), which provided an additional ground truth (higher resolution) structural image to compare our filtering method against (same dataset as Fig. 2). When applied to living tissue, we observe a dramatic reduction in grid-like artifacts at the native focal plane compared to conventional LFM reconstruction (i.e., no filter), as shown in Fig. S6C. Comparing volumetric contrast in standard and *k*-space filtered reconstruction, we see a dip near the native focal plane (Fig. S6B). This is to be expected, as the grid-like patterns lead to an artificial increase in contrast. Similar to the experimentally measured PSFs, line intensity profiles along filtered blood vessels show an important decrease in spurious spatial signal without loss of resolution (Fig. S6D), alteration of structural features, or additional artifacts (Fig. S6F).

## Light-field reconstruction



## *k*-space filtering

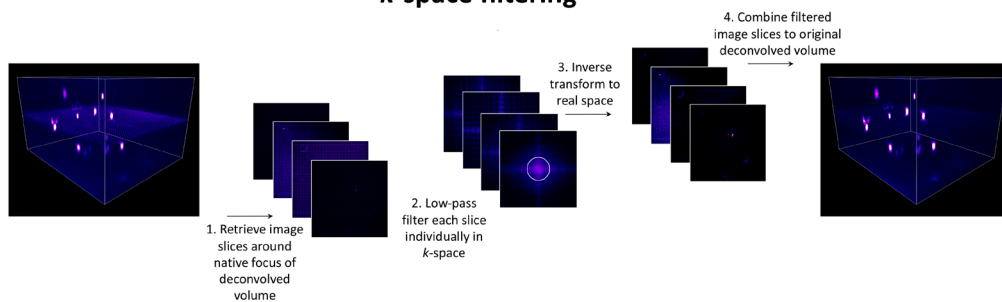


Fig. S4. *k*-space filtering algorithm. LFM (top) reconstructs a complete 3D volume with depth-dependent resolution and artifacts near the native focal plane [5,6]. Due to the non-uniform resolution across the entire volume, a single cutoff frequency cannot be applied without compromising peak resolution at other image planes. *k*-space filtering (bottom) splits the deconvolved volume into smaller subvolumes, and independently processes the subvolume that extends across the native focal plane. Retrieved image slices are low-pass filtered in Fourier (*k*) space, based on the experimental optical transfer function (OTF) bounds at that subvolume. Next, image slices are inverse transformed back into real space, and a median filter is applied to minimize ringing artifacts. The filtered image slices are then combined to assemble the final, denoised volume.

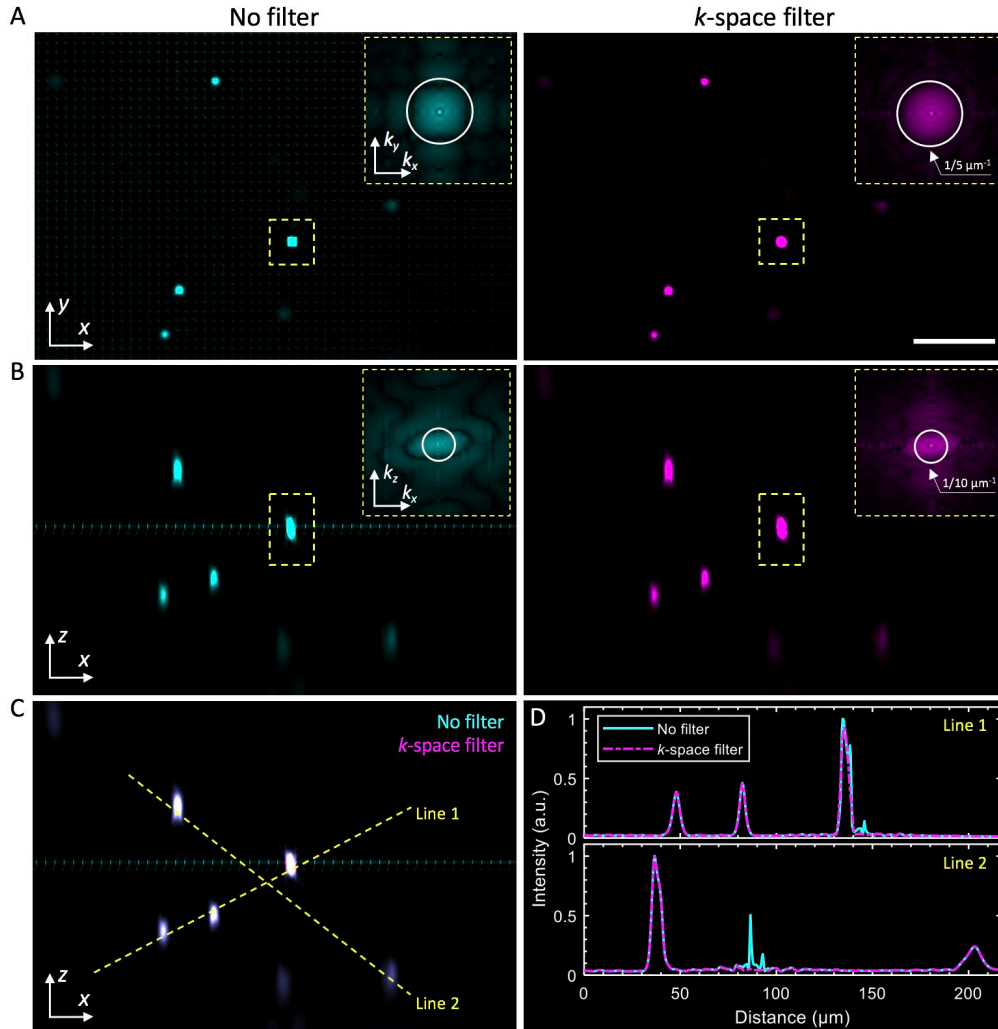


Fig. S5. *k*-space filtering reduces artifacts and improves volume reconstruction with uncompromised resolution. Comparative *x*-*y* (A) and *x*-*z* (B) MIPs of a 300- by 200- by 200- $\mu\text{m}$  sparse field of fluorescent beads before (left column) and after filtering in *k*-space (right column). Each inset shows the spatial frequency content of the corresponding axially-centered PSF at the native focus, as indicated by the dashed yellow rectangle in the image. Both real and frequency space representations show the ability of *k*-space filtering to reduce high-frequency artifacts, laterally and axially. OTF images were equally gamma-contrast-adjusted to aid in visualizing weak features. Scale bar, 50  $\mu\text{m}$ . (C) Overlap of *x*-*z* MIPs show excellent spatial correspondence of PSFs before and after filtering. (D) Comparative line profiles as indicated by the yellow lines in (C). As expected, there is no appreciable loss of resolution by *k*-space filtering (line 1). Away from the native focus, bead-measured signal intensities show full quantitative correspondence, while at the native focal plane, periodic reconstruction artifacts are effectively suppressed (line 2).

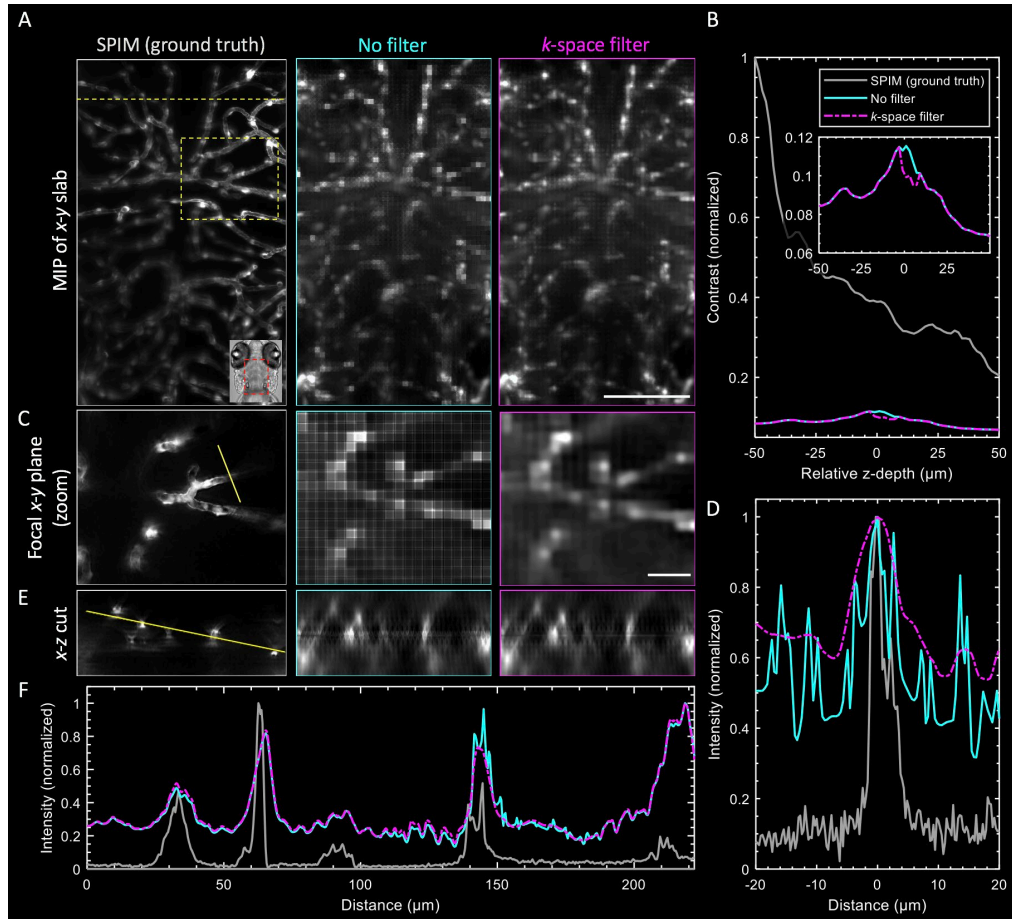


Fig. S6. *k*-space filtering improves volume reconstruction quality *in vivo*. (A) *x-y* MIP of a 100- $\mu\text{m}$ -thick slab (same dataset as Fig. 2), comparing each protocol as shown. Scale bar, 100  $\mu\text{m}$ . (B) Quantification of image contrast versus *z*-depth; each *x-y* slice (from all protocols) was normalized against the deconvolved SPIM (gray) slice at  $z = -50$   $\mu\text{m}$ . Inset shows light-field protocols only, with the expected decrease in artificially high contrast by *k*-space filtering. (C) Focal *x-y* plane (zoom) of yellow boxed region in (A), showing a significant decrease in common reconstruction artifacts by *k*-space filtering (third column). Scale bar, 25  $\mu\text{m}$ . (D) Comparative intensity profiles for each protocol, indicated by line cut in (C). (E) *x-z* slice, at the location indicated by the dashed yellow line in the MIP slab in (A). (F) Comparative intensity profiles for each protocol, indicated by the 225- $\mu\text{m}$  yellow line in (E).

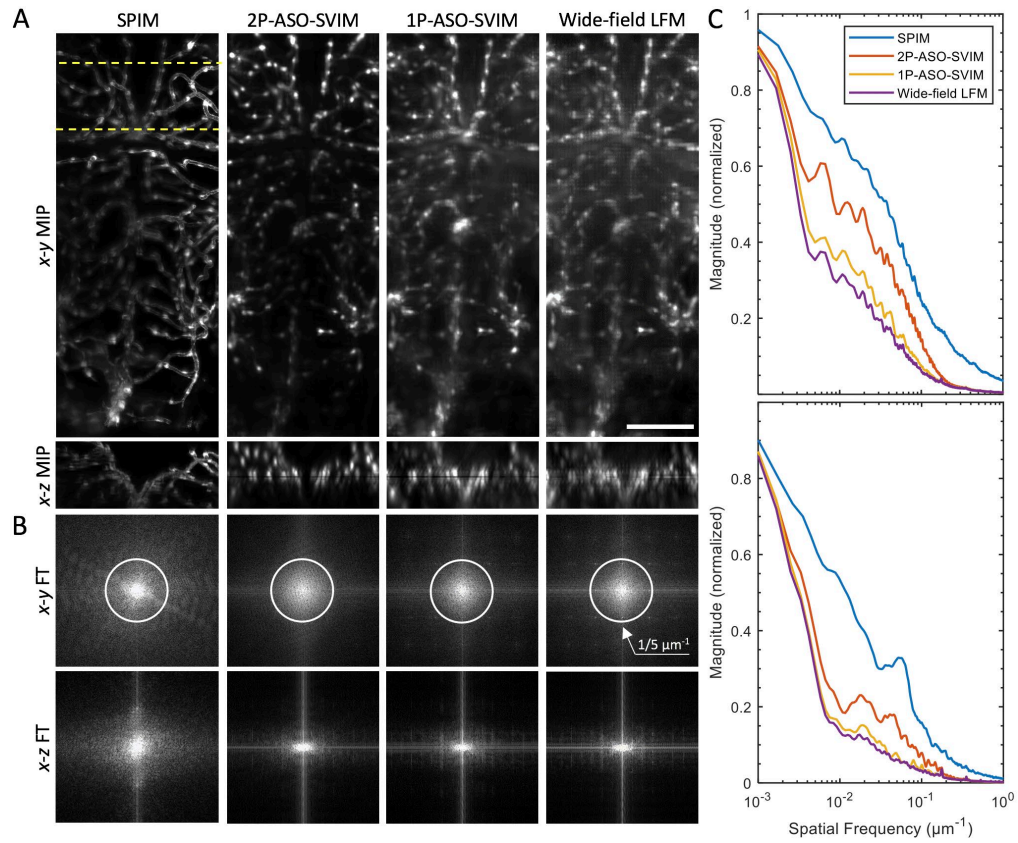


Fig. S7. ASO-SVIM enhances effective resolution across large tissue volumes. (A)  $x-y$  (top row) and  $x-z$  (bottom row) MIPs of a 100- $\mu\text{m}$  thick slab (same dataset as Fig. 2), highlighting maximum attenuation for each modality shown. Scale bar, 100  $\mu\text{m}$ . (B) Fourier transforms (FTs) of the MIPs in (A). Resolution bands (white circles) indicate increased spatial frequency content with ASO-SVIM compared to wide-field illumination, due to decreased out-of-volume background by selective excitation. (C) Average amplitudes along the  $k_x$  (top) and  $k_z$  (bottom) direction of FTs in (B), respectively. Frequency spectra demonstrate the slower spatial frequency roll-off for ASO-SVIM, both laterally and axially, and hence improved effective 3D resolution over the conventional wide-field technique. See also Fig. 2 and Fig. S8.

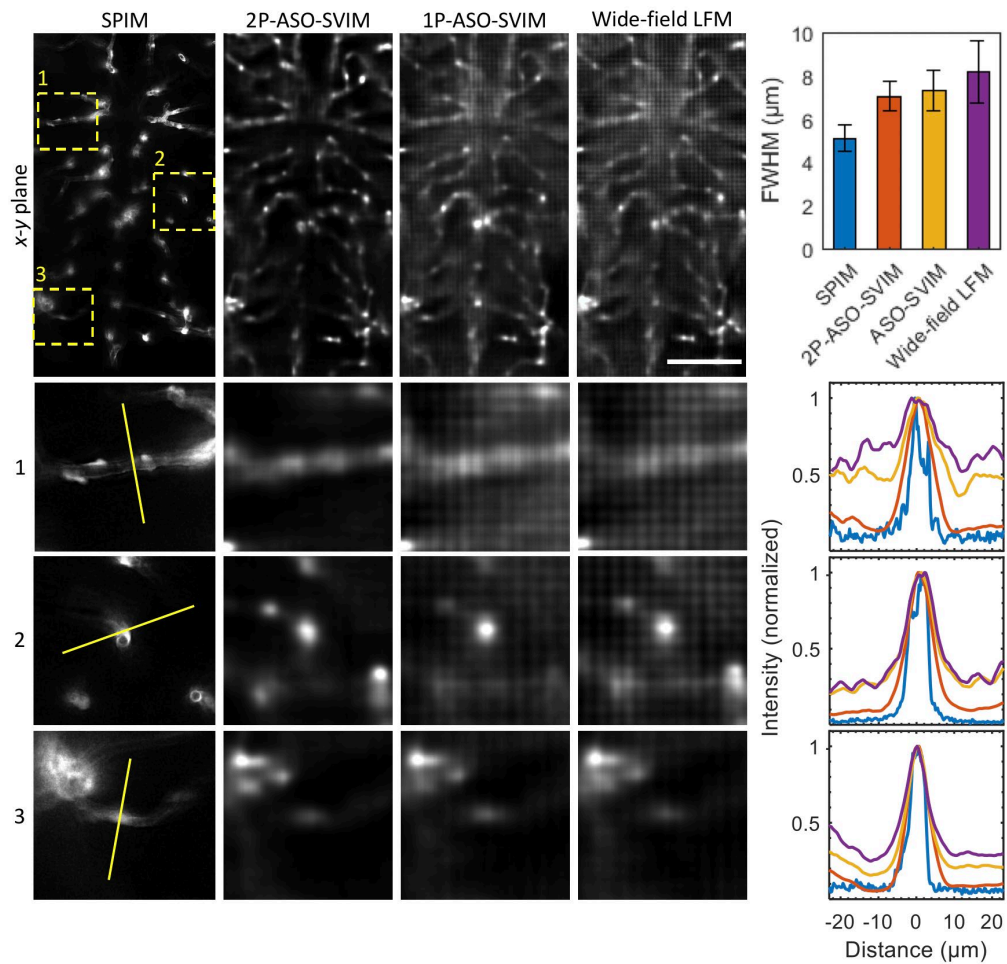


Fig. S8. Comparison of line cuts through vessel structures *in vivo*. Top row:  $x$ - $y$  slice from a 100- $\mu\text{m}$  thick slab (same dataset as Fig. 2), centered at approximately 86  $\mu\text{m}$  into the specimen ( $z = -14 \mu\text{m}$ ), comparing the performance of the indicated modalities. Remaining rows: Zoomed-in regions of structures in the yellow boxes in the  $x$ - $y$  plane (top row), along with corresponding line intensity profiles (as shown by the 50- $\mu\text{m}$  yellow line in the images) plotted on the right. Given the intrinsically higher spatial resolution of SPIM, full quantitative correspondence of the light-field-based images is not expected. All three line profiles were used to quantify the average FWHM and standard deviation for each modality (right column, top). Of the light-field-based methods, 2P-ASO-SVIM achieves the highest biological resolution (owing to nonlinear excitation as well as reduced background and scattering), approaching the performance of SPIM, followed by ASO-SVIM in 1P mode, and last, wide-field LFM. Note that this plane is not  $k$ -space filtered. Scale bar, 100  $\mu\text{m}$ . See also Fig. 2 and S7.

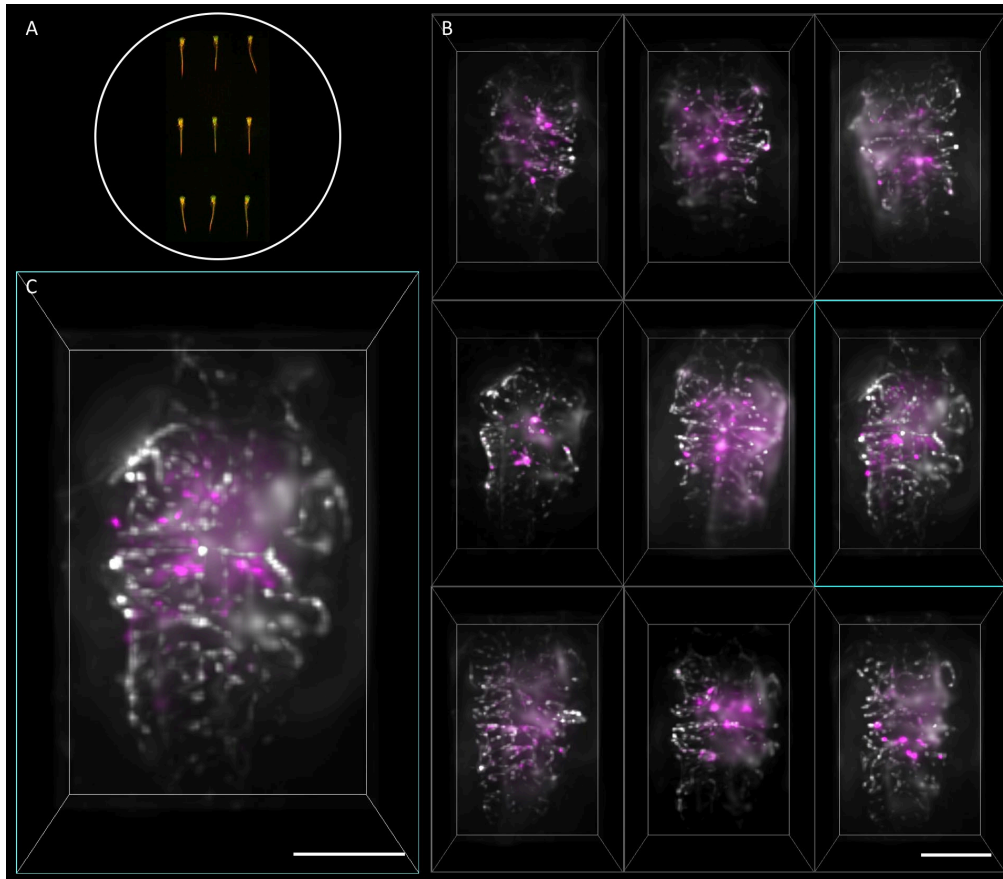
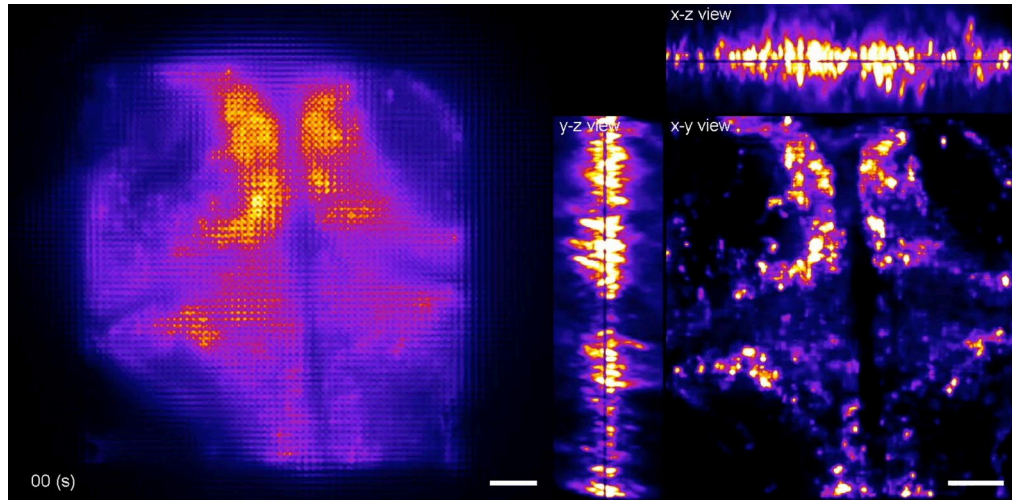
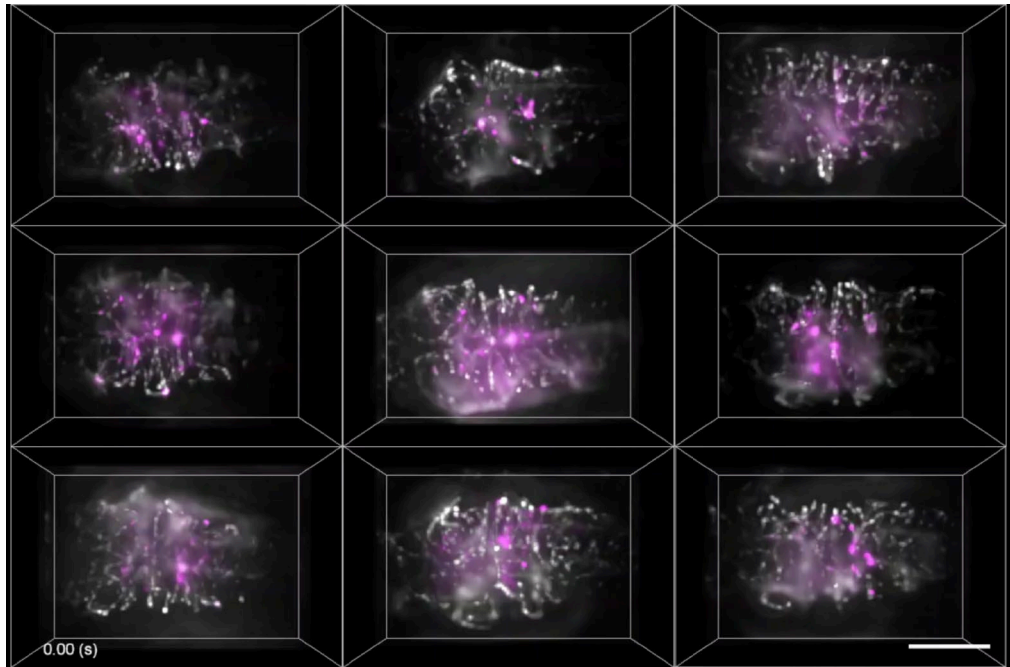


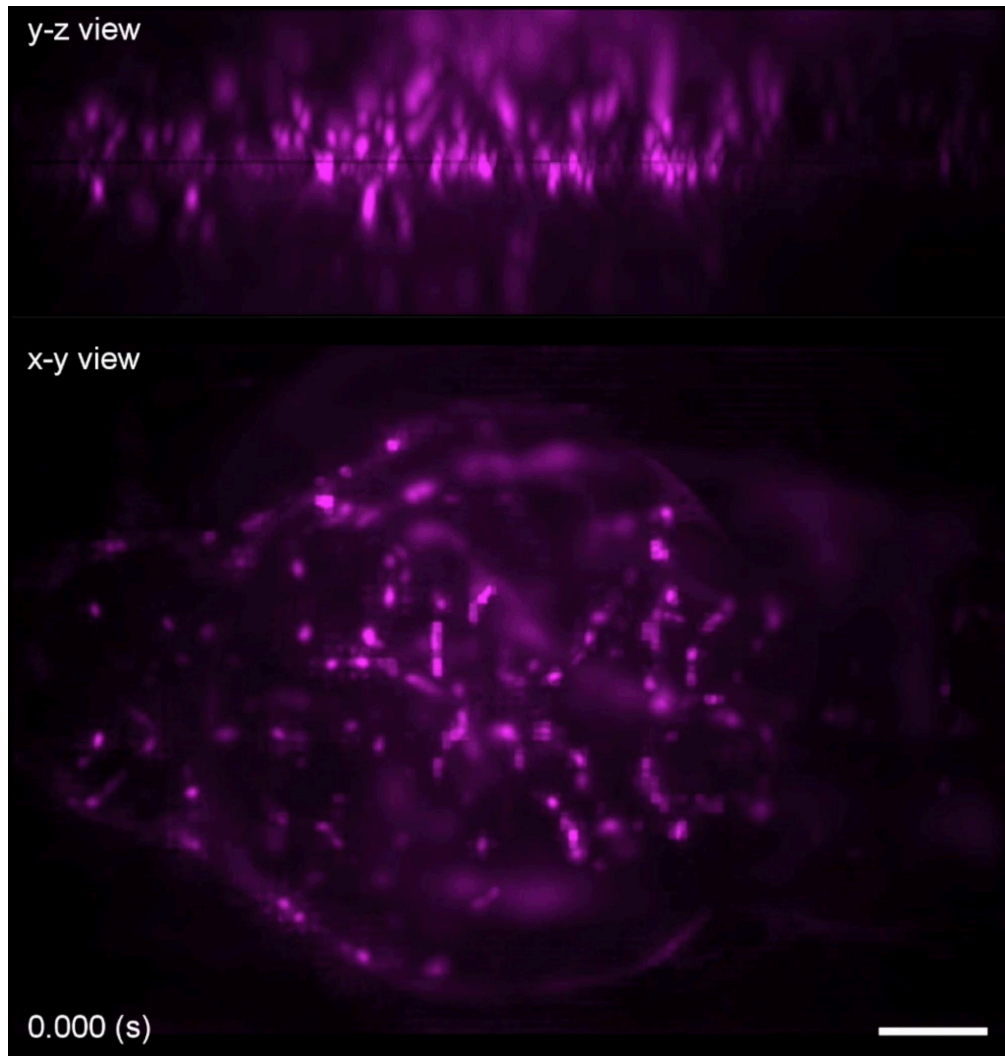
Fig. S9. ASO-SVIM enables high-throughput imaging of whole-brain blood flow in zebrafish larvae. (A) Nine 5-dpf zebrafish, with fluorescent labels in both the blood cells [Tg(gata1:dsRed)] and endocardium [Tg(kdr1:eGFP)], were mounted in a standard multi-well plate. Two-color imaging was performed over a synchronous 670- by 470- by 200- $\mu\text{m}$  volume at  $\sim 50$  Hz, per color, for each fish. (B) MIPs of 50- $\mu\text{m}$ -thick slabs axially-centered within the 9 dually-labeled zebrafish brains. Captured light-fields were reconstructed using ray optics [3] for increased computational speed. Blood cells and endocardium are represented in magenta and grayscale, respectively. Scale bar, 200  $\mu\text{m}$ . (C) Magnified MIP of the specimen highlighted by the cyan box in (B). Scale bar, 100  $\mu\text{m}$ . See Visualizations 2-4.



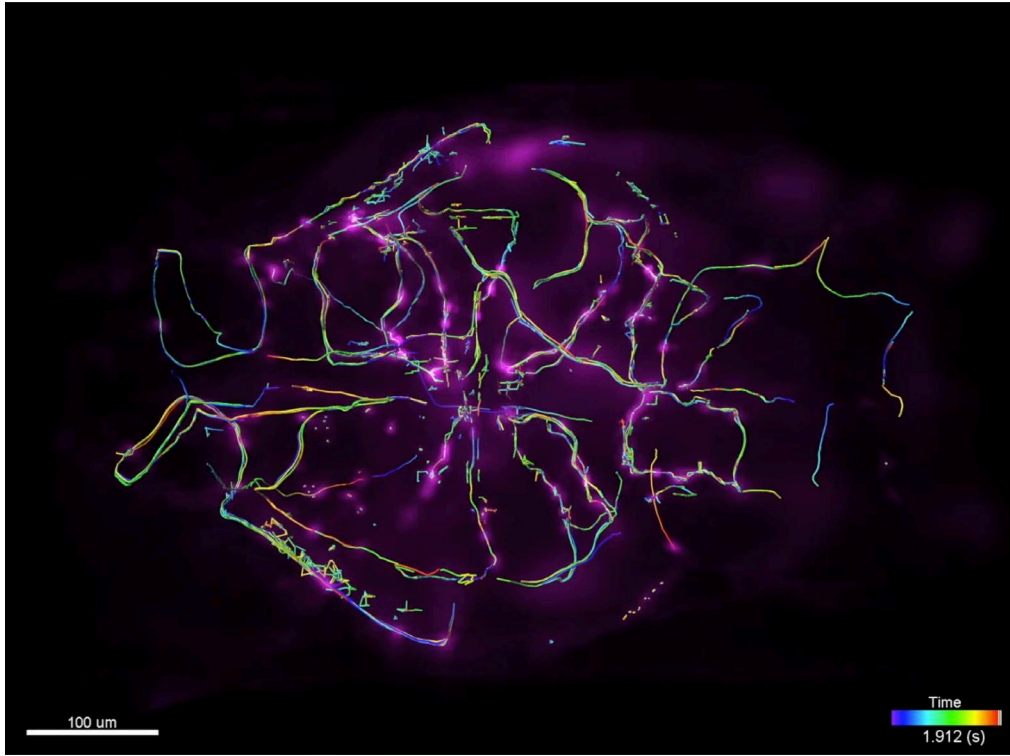
Visualization 1. Fluorescence light-field (left) and 3D reconstructed maximum-intensity projections along the indicated directions (right) of a time-lapse recording of brain-wide neural activity in a 5-dpf transgenic zebrafish. 2P-ASO-SVIM imaging was performed at a volumetric rate of 1 Hz. Same dataset as presented in Fig. 3. Scale bar (left), 150  $\mu\text{m}$ , (right) 50  $\mu\text{m}$ .



Visualization 2. Maximum-intensity projections of nine 5-dpf zebrafish, with fluorescent labels in both the blood cells [Tg(gata1:dsRed)] and endocardium [Tg(kdrl:eGFP)], represented in magenta and grayscale, respectively. Samples were recorded serially, with each sample imaged with 1P-ASO-SVIM over a synchronous 670- by 470- by 200- $\mu\text{m}$  volume at  $\sim 50$  Hz. Same dataset as presented in Fig. S9. Scale bar, 200  $\mu\text{m}$ .



Visualization 3. 1P-ASO-SVIM imaging of blood cells [Tg(gata1:dsRed)] flowing across the entire brain of a 5-dpf zebrafish. Cellular resolution imaging was performed over a 670- by 470- by 200- $\mu\text{m}$  volume at  $\sim 50$  Hz. Fluorescent light-fields were wave optics reconstructed. Animal is oriented anterior (left) to posterior (right). Scale bar, 50  $\mu\text{m}$ .



Visualization 4. Volumetric view of whole-brain blood flow, with red blood cell tracks color-coded in time. Same dataset as presented in Visualization 3.

## References

1. T.V. Truong, D.B. Holland, S. Madaan, A. Andreev, K. Keomanee-Dizon, J.V. Troll, D.E.S. Koo, M.J McFall-Ngai, and S.E. Fraser, "High-contrast, synchronous volumetric imaging with selective volume illumination microscopy," *Communications Biology* **3**, 1-8 (2020).
2. V. Chauhan, P. Bowlan, J. Cohen, and R. Trebino, "Single-diffraction-grating and grism pulse compressors," *Appl. Opt.* **27**, 619 (2010).
3. V. Maioli, A. Boniface, P. Mahou, J. F. Ortas, L. Abdeladim, E. Beaurepaire, and W. Supatto, "Fast *in vivo* multiphoton light-sheet microscopy with optimal pulse frequency," *Biomed. Opt. Express* **11**, 6012-6026 (2020).
4. M. Levoy, R. Ng, A. Adams, M. Footer, and M. Horowitz, "Light field microscopy," in *Proceedings of ACM SIGGRAPH* (ACM, 2006) p. 924-934.
5. M. Broxton, L. Grosenick, S. Yang, N. Cohen, A. Andalman, K. Deisseroth, and M. Levoy, "Wave optics theory and 3-D deconvolution for the light field microscope," *Optics Express* **21**, 25418-25439 (2013).
6. R. Prevedel, Y. G. Yoon, M. Hoffmann, N. Pak, G. Wetzstein, S. Kato, T. Schrödel, R. Raskar, M. Zimmer, E. S. Boyden, and A. Vaziri, "Simultaneous whole-animal 3D imaging of neuronal activity using light-field microscopy," *Nature Methods* **11**, 727-730 (2014).
7. K. Keomanee-Dizon, S.E. Fraser, and T.V. Truong, "A versatile, multi-laser twin-microscope system for light-sheet imaging," *Review of Scientific Instruments* **91**, 053703 (2020).
8. C. Dunsby, "Optically sectioned imaging by oblique plane microscopy," *Opt. Express* **16**, 20306-20316 (2008).
9. M. Kumar, S. Kishore, J. Nasenbeny, D. L. McLean, and Y. Kozorovitskiy, "Integrated one- and two-photon scanned oblique plane illumination (SOPi) microscopy for rapid volumetric imaging," *Opt. Express* **26**, 13027-13041 (2018).
10. V. Voleti, K. B. Patel, W. Li, C. P. Campos, S. Bharadwaj, H. Yu, C. Ford, M. J. Casper, R. W. Yan, W. Liang, C. Wen, K. D. Kimura, K. L. Targof, E. M. C. Hillman, "Real-time volumetric microscopy of *in vivo* dynamics and large-scale samples with SCAPE 2.0," *Nature Methods* **16**, 1054 (2019).
11. B. Yang, X. Chen, Y. Wang, S. Feng, V. Pessino, N. Stuurman, N.H. Cho, K.W. Cheng, S.J. Lord, L. Xu, D. Xie, R.D. Mullins, M.D. Leonetti, and B. Huang, "Epi-illumination SPIM for volumetric imaging with high spatial-temporal resolution," *Nature Methods* **16**, 501-504 (2019).
12. A. Millett-Sikking and A.G. York, "High NA single-objective light-sheet" doi: 10.5281/zenodo.3244420 (2019).
13. E. Sapoznik, B. J Chang, J. Huh, R. J. Ju, E. V. Azarova, T. Pohlkamp, E. S. Welf, D. Broadbent, A. F. Carisey, S. J. Stehbens, K. M. Lee, A. Marín, A. B. Hanker, J. C. Schmidt, C. L. Arteaga, B. Yang, Y. Kobayashi, P. R. Tata, R. Kruthoff, K. Doubrovinski, D. P. Shepherd, A. Millett-Sikking, A. G. York, K. M. Dean, R. P. Fiolka, "A versatile oblique plane microscope for large-scale and high-resolution imaging of subcellular dynamics," *eLife* **9**, e57681 (2020).
14. T.A. Pologruto, B.L. Sabatini, and K. Svoboda, "ScanImage: flexible software for operating laser scanning microscopes," *Biomedical engineering online* **2**, 13 (2003).
15. A. D. Edelstein, M. A. Tsuchida, N. Amodaj, H. Pinkard, R. D. Vale, and N. Stuurman, "Advanced methods of microscope control using  $\mu$ Manager software," *Journal of Biological Methods* **1**, 10 (2015).